

Word and bit line operation of a $1 \times 1 \mu\text{m}^2$ superconducting vortex-based memory

Taras Golod, Lise Morlet-Decarnin, and Vladimir M. Krasnov*

Department of Physics, Stockholm University, AlbaNova University Center, SE-10691 Stockholm, Sweden.

The lack of dense random access memory is one of the main bottlenecks for the creation of a digital superconducting computer. In this work we study experimentally vortex-based superconducting memory cells. Three main results are obtained. First, we test scalability and demonstrate that the cells can be straightforwardly miniaturized to submicron sizes. Second, we emphasize the importance of conscious geometrical engineering. In the studied devices we introduce an asymmetric easy track for vortex motion and show that it enables a controllable manipulation of vortex states. Finally, we perform a detailed analysis of word and bit line operation of a $1 \times 1 \mu\text{m}^2$ cell. High-endurance, non-volatile operation at zero magnetic field is reported. Remarkably, we observe that the combined word and bit line threshold current is significantly reduced compared to the bare word-line operation. This could greatly improve the selectivity of individual cell addressing in a multibit RAM. The achieved one square micron area is an important milestone and a significant step forward towards creation of a dense cryogenic memory.

I. INTRODUCTION

The development of superconducting (SC) electronics could lead to a breakthrough in future computation techniques. Major advances in the creation of a SC quantum computer were recently achieved [1, 2]. However, practical calculations today are made on a classical computer and demands for digital computation capacities are growing in the explosive manner. Resistivity causes principle limitations for semiconductor-based electronics. The large resistance, R , of silicon transistors both limits the operation speed (determined by the RC time constant) and creates a problem of heat management in very-large-scale-integration (VLSI) circuits. Those obstacles can be obviated by shifting to superconductors with $R = 0$. The maximum operation frequency of SC electronics is determined by the energy gap, which can exceed 10 THz in high-temperature SCs [3]. For large data facilities, shifting from semiconductors to superconductors could drastically improve both the power efficiency (by an order of magnitude) and the computation speed (by several orders of magnitude). Such perspectives reignited the interest to a classical SC computer [4–12].

Digital SC electronics has a long history. Rapid-single-flux-quantum (RSFQ) architecture was developed almost half a century ago [13]. It is based on storage and manipulation of the flux quantum, Φ_0 , in superconducting quantum interference devices (SQUIDs). Nb-based RSFQ electronics is capable of operation up to ~ 200 GHz frequency [4], two orders of magnitude faster than modern computers. However, RSFQ has a major problem with scalability. The current needed for introduction of Φ_0 is determined by the inductance, L , of the SQUID loop, $I = \Phi_0/L$. Upon miniaturization, L decreases and the operation current increases inversely proportional to the size. Therefore, RSFQ is not compatible with the VLSI technology. The main bottleneck is the lack of

dense random-access memory (RAM) [4–6]. State of the art RSFQ RAM has a footprint of $\sim 100 \mu\text{m}^2$ per bit [5, 11, 12, 14]. Large sizes cause significant delay times. In fact, the speed of RSFQ is limited by delay times, rather than the energy gap [4].

Novel approaches are needed for building a VLSI-competitive SC electronics. Several strategies for making dense SC RAM have been suggested recently [7, 15–29]. In Ref. [7] it was shown that a single Abrikosov vortex (AV) can be used as an information carrier. AV represents the smallest magnetic object in a superconductor, enabling miniaturization to submicron sizes. Prototypes of single-bit AVRAM cells with excellent performance were demonstrated [7]. However, the way from a single cell to a dense multi-bit RAM is full of hazards, as could be learned from the history of MRAM [30]. Crosstalk between cells could hamper RAM operation. It could be mitigated by a highly selective word and bit line (WL & BL) addressing of individual cells. So far WL & BL operation of AVRAM cells has not been analyzed.

In this work we study experimentally Nb-based AVRAM cells. Our aim is threefold. First, we study scalability. Cells with the same geometry, but different sizes 5, 3 and $1 \mu\text{m}$ are tested. We confirm that AVRAM cells are scalable to submicron sizes, while keeping robust non-volatile operation at zero magnetic field. Second, we emphasize the importance of conscious geometrical design for the optimization of cells. In the studied cells, we introduce an asymmetric “easy track” for vortex motion. It removes the degeneracy between vortex and antivortex states and, thus, facilitates controllable operation of the cell. Finally, we analyze the word and bit line operation of a $1 \times 1 \mu\text{m}^2$ cell. We observe that simultaneous application of WL and BL pulses can significantly reduce threshold currents for vortex manipulation. Such a cooperative WL & BL effect could greatly improve the selectivity of addressing in a multibit RAM. We conclude that AVRAM is a feasible candidate for the creation of dense cryogenic memory.

* vladimir.krasnov@fysik.su.se

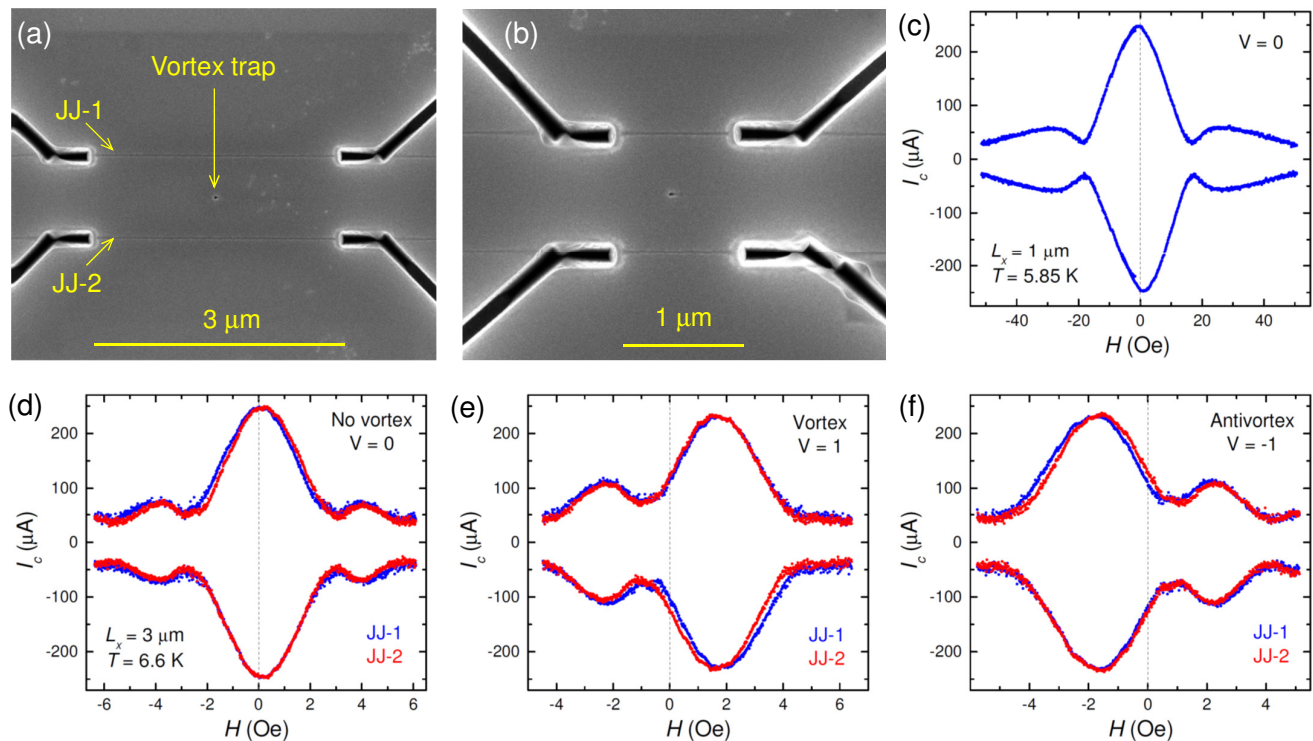


FIG. 1. **Demonstration of AVRAM cell scalability.** (a) and (b) SEM images of two cells with sizes (a) $L_x \simeq 3 \mu\text{m}$, and (b) $L_x \simeq 1 \mu\text{m}$. (c) Magnetic field modulation of the critical current in a readout junction on the $L_x = 1 \mu\text{m}$ cell in the vortex free state, $V=0$. (d-f) $I_c(H)$ modulations for both junctions on the $L_x = 3 \mu\text{m}$ cell: (d) in the vortex-free state, $V=0$, (e) with a trapped vortex, $V=1$, and (f) with an antivortex $V=-1$.

II. RESULTS

A. Samples

Planar AVRAM cells are made from a single Nb film of thickness $d = 70 \text{ nm}$. The film was deposited on an oxidized Si substrate by magnetron sputtering. First, a $\sim 5 \mu\text{m}$ cross-like structure was made by photolithography and reactive ion etching. Subsequently, the sample was transferred into a dual-beam $^+ \text{Ga}$ Focused Ion Beam (FIB) and two planar readout Josephson junctions (JJs), of variable-thickness type, were made by cutting narrow grooves in Nb. Finally, a vortex trap, a nano-scale hole, was made in the electrode between the JJs. More details about junction fabrication and characterization can be found in Refs. [7, 31–33]. The fabrication procedure is highly reproducible and the characteristics of both JJs are practically identical. Several devices with similar geometry but different lengths of readout JJs, $L_x = 5, 3$ and $1 \mu\text{m}$, were made simultaneously on the same chip. Measurements are performed in a closed-cycle cryostat. Magnetic field, perpendicular to the Nb film was supplied by a superconducting magnet. We can controllably introduce and remove vortices by short current pulses, as described in Refs. [7, 34]. Additional information can be found in the Supplementary material [34].

B. Miniaturization

Figures 1 (a) and (b) show scanning electron microscope (SEM) images of the cells with (a) $L_x = 3 \mu\text{m}$ and (b) $L_x = 1 \mu\text{m}$. Figs. 1 (c) and (d) show magnetic field dependencies of critical currents, $I_c(H)$, for the two devices in the vortex-free state, $V=0$. All JJs exhibit Fraunhofer-type modulation with the central maximum at $H = 0$. The flux quantization field for the $1 \mu\text{m}$ device (c) is approximately 7 times larger than for the $3 \mu\text{m}$ device (d), consistent with the expected difference in flux quantization areas [33, 34]. The largest cells, $L_x = 5 \mu\text{m}$, are similar to those, studied in Ref. [7]. Their characteristics can be found in the Supplementary [34].

In Figs. 1 (e) and (f) we show $I_c(H)$ patterns for both readout JJs on the $3 \mu\text{m}$ cell with a trapped vortex (e), or an antivortex (f). From Figs. 1 (d-f) it is seen that the three primary states with different vorticities, (d) $V=0$, (e) $V=1$ and (f) $V=-1$, are clearly distinguishable. Vortex trapping leads to a characteristic distortion of $I_c(H)$ [7, 31, 35–37], and to a threefold reduction of $I_c(H = 0)$. This enables a simple recognition and readout of vortex states. The closer the AV is to the JJ, the larger is the junction response [35]. In these cells, the vortex trap is placed symmetrically with respect to the JJs; see Fig. 1 (a). Consequently, the responses of both JJs are identical

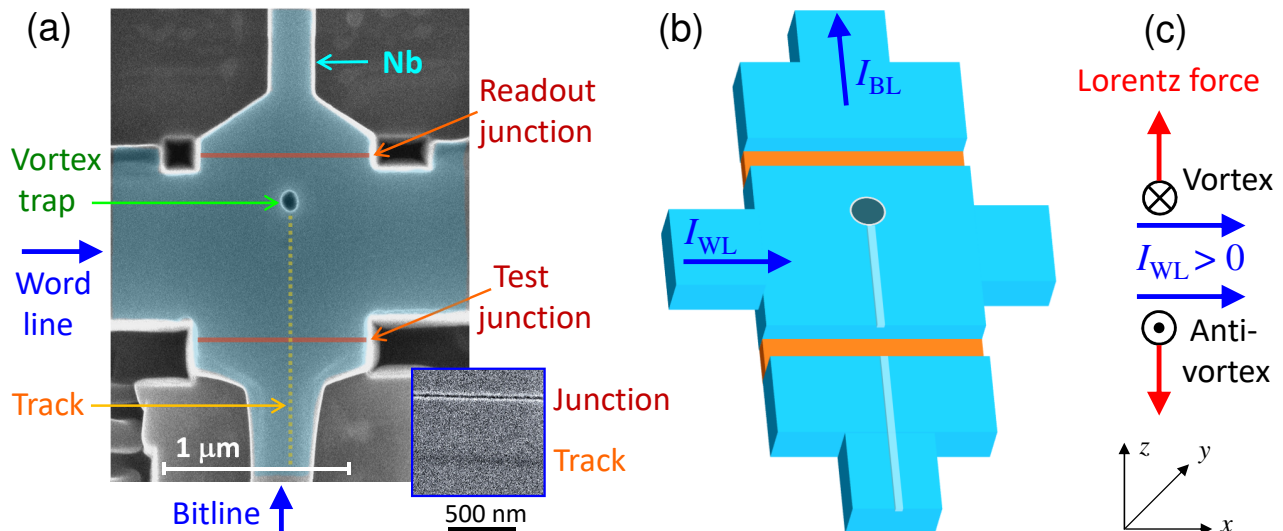


FIG. 2. **Geometry of a $1 \times 1 \mu\text{m}^2$ cell with word and bit lines.** (a) SEM image of the device (false color). Inset shows a SEM image of a junction groove and a FIB track for another device. (b) A sketch of the cell with indicated directions of wordline and bitline currents. (c) Direction of Lorentz forces, exerted on a vortex and an antivortex by a positive WL current. The easy operation with a small WL threshold current is expected when the vortex is transported along the track.

and $I_c(H)$ patterns for both JJs merge in Figs. 1 (e) and (f). Such a coincidence confirms that the vortex is indeed placed in the trap. We always use two JJs in our AVRAM cells: one for determining the state (the readout JJ) and the other for confirming that the vortex is located in the trap (the test JJ).

In Figures 2 (a) and (b) we show a SEM image and a sketch of a $\sim 1 \times 1 \mu\text{m}^2$ cell, in which excessive parts of the Nb electrode were removed. The trap with a diameter of ~ 100 nm is placed close (~ 240 nm) to the top readout JJ. The bottom, test JJ is at a significantly longer distance (~ 740 nm). The left-right and the bottom-top electrode pares form WL and BL, respectively. Below we will focus on the analysis of this cell.

C. Geometrical asymmetry

Vortex states can be manipulated by current pulses [7]. However, in a symmetric cell, 1 and -1 states are degenerate at $H = 0$. Currents of any direction create both a vortex and an antivortex at opposite sides of the device and drive them inside, where they annihilate. Therefore, operation is impossible in a perfectly symmetric cell. In reality, there is always some asymmetry that lifts the degeneracy. However, the operation can not be fully controllable without conscious geometrical design.

The asymmetry in the device from Fig. 2 (a) is introduced by making an easy track for vortex motion at one side of the trap. It is made by a single scanning of the FIB to/from the trap. The inset in Fig. 2 (a) shows a high-resolution SEM image of the track alongside of the junction groove (for another device). It is seen that the

track makes just a minor depression in the Nb film. It does not form a JJ, but creates an easy path for AV to and from the trap [31]. Fig. 2 (c) indicates directions of Lorentz forces, F_L , exerted on a vortex and an antivortex by a positive WL current. From the comparison with the track position in Fig. 2 (a), it is expected that a positive I_{WL} would easily introduce a vortex ($0 \rightarrow 1$) and remove an antivortex ($-1 \rightarrow 0$) along the easy track. All other operations should be more difficult and require larger threshold currents.

Table I summarizes measured threshold currents for all operations on this cell, performed by sending a single pulse along either WL or BL. For WL operation, we observe three threshold levels $|I_{WL}|$: $\simeq 0.15$ mA (easy), $\simeq 0.73$ mA (moderate) and $\simeq 0.87$ mA (difficult). Of those, the “easy” corresponds to erasing, $\pm 1 \rightarrow 0$, along the track; the “moderate” to writing $0 \rightarrow \pm 1$ along the track; and the “difficult” to all other operations in the direction opposite to the track. Thus, the subtle track is playing a very important role. It introduces the required asymmetry, enabling a controllable realization of all four main operations along the easy path. Control in the “difficult” regime is much worse because such currents can do any operation.

Lorentz forces induced by BL currents are perpendicular to the track. Therefore, there is no profound asymmetry or easy path, and all BL operations are “hard”, $|I_{BL}| > 1$ mA. This is important because the passiveness of BL enables nondestructive readout. As seen from Figs. 2 (a) and (b), BL currents go through the JJs. Since fairly large BL currents do not affect the vortex state, we can nondestructively readout the state by measuring junction voltage and resistance. This is demonstrated in

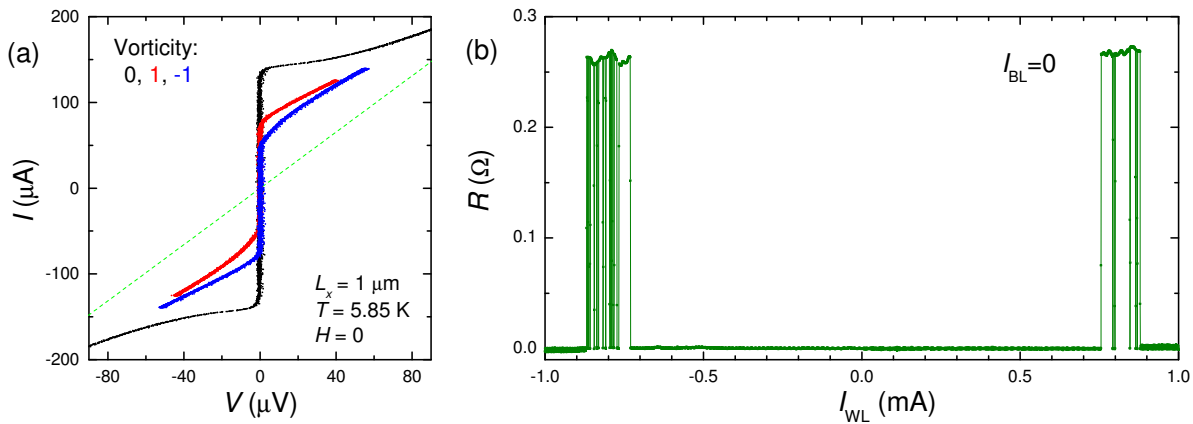


FIG. 3. **Characteristics of the $1 \times 1 \mu\text{m}^2$ cell from Fig. 2 (a).** (a) Current-Voltage characteristics of the readout junction: black - in the vortex-free state, red - with the trapped vortex, and blue - with an antivortex. Green dashed line represents the normal resistance, $R_n = 0.61 \Omega$. (b) Demonstration of the write operation $0 \rightarrow \pm 1$ by wordline pulses (without bitline currents). The readout junction resistance is shown as a function of the WL current pulse amplitude. Measurements were performed at $T = 5.85 \text{ K}$ and $H = 0$.

Operation	Easy	Moderate	Difficult	Hard
write 1 ($0 \rightarrow 1$)		$I_{\text{WL}} > 0$	$I_{\text{WL}} < 0$	BL
write -1 ($0 \rightarrow -1$)		$I_{\text{WL}} < 0$	$I_{\text{WL}} > 0$	BL
erase 1 ($1 \rightarrow 0$)	$I_{\text{WL}} < 0$		$I_{\text{WL}} > 0$	BL
erase -1 ($-1 \rightarrow 0$)	$I_{\text{WL}} > 0$		$I_{\text{WL}} < 0$	BL
Threshold (mA)	0.15	0.73	0.87	> 1

TABLE I. **Summary of single-line operations for the device from Fig. 2 (a) at $T = 5.85 \text{ K}$ and $H = 0$.** WL operations have three distinct levels. Easy ($|I_{\text{WL}}| \simeq 0.15 \text{ mA}$) and moderate ($|I_{\text{WL}}| \simeq 0.73 \text{ mA}$) thresholds correspond to vortex propagation along the easy track. The difficult threshold ($|I_{\text{WL}}| \simeq 0.87 \text{ mA}$) - to vortex motion outside the track. For BL operations there is no easy path; therefore, all BL operations are hard ($|I_{\text{BL}}| > 1 \text{ mA}$).

Figure 3 (a), which shows the current-voltage (I - V) characteristics of the readout JJ in $V=0$ (black), 1 (red) and -1 (blue) states. The current, sent via the BL, does not cause switching between vortex states within this bias range. Thus, the introduced asymmetry is crucial both for controllable operation and for nondestructive readout.

D. Wordline operation

First, we analyze the $0 \rightarrow \pm 1$ write operation solely by the WL current. The experiment is done in the following manner. First, the cell is prepared in the 0-state. After that, a short pulse with an amplitude I_{WL} is sent through the WL. The state of the device is evaluated by measuring the locking resistance, R , of the JJ via the BL. The probe ac current $I_{\text{ac}} \simeq 130 \mu\text{A}$ is smaller than I_c in the 0-state, but larger than in 1 and -1 states (see Fig. 3 (a)), so that the 0-state corresponds to $R = 0 \Omega$, and 1 and -1 states to $R \simeq 0.27$ and 0.26Ω , respectively. Fig. 3 (b) shows the readout JJ resistance as a function

of I_{WL} . It is seen that vortices can be written in the range $0.73 \text{ mA} \lesssim |I_{\text{WL}}| \lesssim 0.87 \text{ mA}$. The lower limit, $|I_{\text{WL}}| \simeq 0.73 \text{ mA}$, corresponds to the “moderate” threshold for writing along the track. As follows from Table I, positive I_{WL} causes $0 \rightarrow 1$ switching, and negative $0 \rightarrow -1$ switching. At $|I_{\text{WL}}| > 0.87 \text{ mA}$, no switching is observed. Presumably, this is caused by exceeding the “difficult” threshold, which leads to the introduction of an opposite vortex, that annihilates with the one trapped earlier via the track.

In Fig. 4, we show representative examples of high-endurance operations by periodic positive/negative WL pulses. In Fig. 4 (a), a positive pulse, $I_{\text{WL}} = 0.75 \text{ mA}$, slightly above the “moderate” threshold, writes a vortex ($0 \rightarrow 1$) and a small negative pulse, $I_{\text{WL}} = 187.5 \mu\text{A}$, erases it. Both operations occur along the track. However, erasing is significantly easier than writing.

In Fig. 4 (b), a negative pulse, $I_{\text{WL}} = -0.8 \text{ mA}$, writes an antivortex ($0 \rightarrow -1$). The subsequent positive pulse, $I_{\text{WL}} = 1.0 \text{ mA}$, above the “difficult” threshold, annihilates it and switches the cell into the 0-state. The next similar pulse doesn’t cause switching from the 0-state, consistent with Fig. 3 (b).

In Fig. 4 (c), a 4-pulse train with small $\pm 0.2 \text{ mA}$ and moderate $\pm 0.8 \text{ mA}$ pulses is applied. Here, the moderate negative/positive pulses write $-1/1$, and subsequent small positive/negative pulses erase them. All operations are achieved via the easy track.

Fig. 4 (d) represents a similar 4-pulse train with $\pm 0.15 \text{ mA}$ and $\pm 0.8 \text{ mA}$ pulses. Here the small negative pulse appears to be sub-threshold and does not erase the 1-state. The subsequent moderate negative pulse causes $1 \rightarrow -1$ switching, which can be considered as a sequential entrance of two antivortices, of which the first annihilates with the trapped vortex and the second stays in the trap. The small positive pulse, however, is sufficient

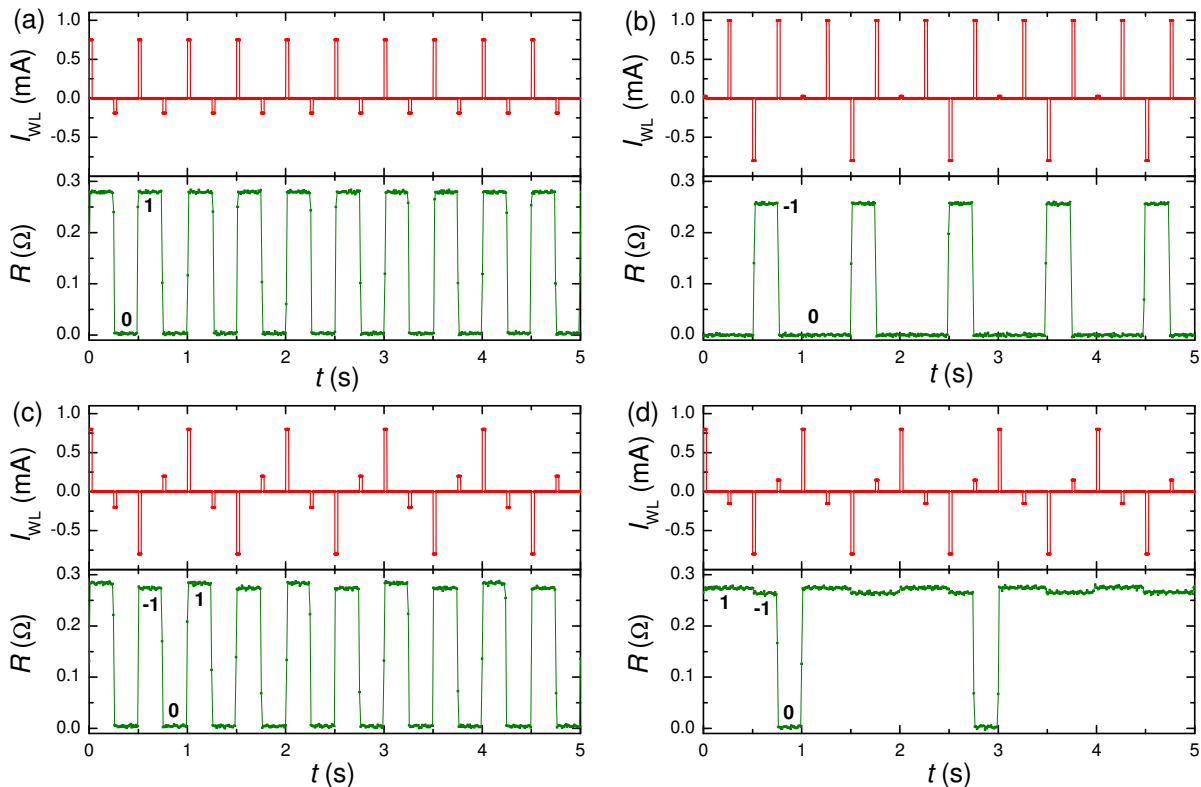


FIG. 4. **Demonstration of wordline operation of the $1 \times 1 \mu\text{m}^2$ cell (without bitline currents).** (a) Writing and erasing a vortex along the easy path by WL pulses 0.75 and -0.1875 mA. (b) Writing an antivortex along the easy path and erasing along the difficult path by WL pulses -0.8 and 1.0 mA. (c) Writing and erasing vortices and antivortices along the easy path by WL pulses ± 0.8 and ± 0.2 mA. (d) The same as in (c) with WL pulses ± 0.8 and ± 0.15 mA. In all figures, top panels show time sequences of WL pulses and bottom panels - a simultaneously measured ac-resistance of the readout junction. Measurements were performed at $T = 5.85$ K and $H = 0$.

for erasing the -1 state. The small asymmetry between 1 and -1 states, also seen from the I - V s in Fig. 3 (a), is caused either by a tiny residual field in the cryostat or by a current-induced self-field effect [32]. This allows a distinction between 1 and -1 states, as can be seen in the bottom panel of Fig. 4 (d).

E. Word and Bit-line operation

A multi-bit RAM requires selective addressing of individual cells by coincident WL and BL pulses. Figure 5 demonstrates the WL+BL write operation, $0 \rightarrow \pm 1$. JJ resistance is shown as a function of the positive WL amplitude for several values of BL pulses: (a) $I_{BL} = \pm 70 \mu\text{A}$, (b) $I_{BL} = \pm 220 \mu\text{A}$, and (c) $I_{BL} = \pm 300 \mu\text{A}$. It is seen that the threshold WL current is reducing with increasing the BL current. Remarkably, the WL+BL operation leads to a significant reduction of the total threshold current, $I_{tot} = |I_{WL}| + |I_{BL}|$: $I_{tot} \simeq 730 \mu\text{A}$ for $I_{BL} = 0$ (see Fig. 3) and $\pm 70 \mu\text{A}$; $I_{tot} \simeq 520 \mu\text{A}$ for $I_{BL} = \pm 220 \mu\text{A}$; and $I_{tot} \simeq 320 - 400 \mu\text{A}$ for $I_{BL} = \pm 300 \mu\text{A}$. The latter is approximately two times

smaller than for a solo WL operation. Thus, the cooperative effect of WL and BL pulses is significantly better than a sum of the two currents. This is very good because it can greatly improve the selectivity of addressing individual cells in a multi-bit AVRAM.

Fig. 6 demonstrates switching dynamics with WL and BL pulses. Panel (a) shows low-threshold switching. Here a small $I_{BL} = -300 \mu\text{A}$ together with a very small $I_{WL} = 29 \mu\text{A}$ causes $0 \rightarrow -1$ switching and a small $I_{WL} = 200 \mu\text{A}$ erases it, $-1 \rightarrow 0$. Subsequent WL-only pulses with the same amplitudes, 29 and $200 \mu\text{A}$, do not affect the 0-state. In panel (b), similar write and erase pulses are applied. Negative WL-only pulses -200 and $-800 \mu\text{A}$, applied in the -1 state, do not affect the state. Even larger BL-only pulses, $|I_{BL}| > 1$ mA, can be applied without changing the state of the device (see Table I). This illustrates that the smallness of the combined WL+BL current does not affect the robustness of non-destructive readout.

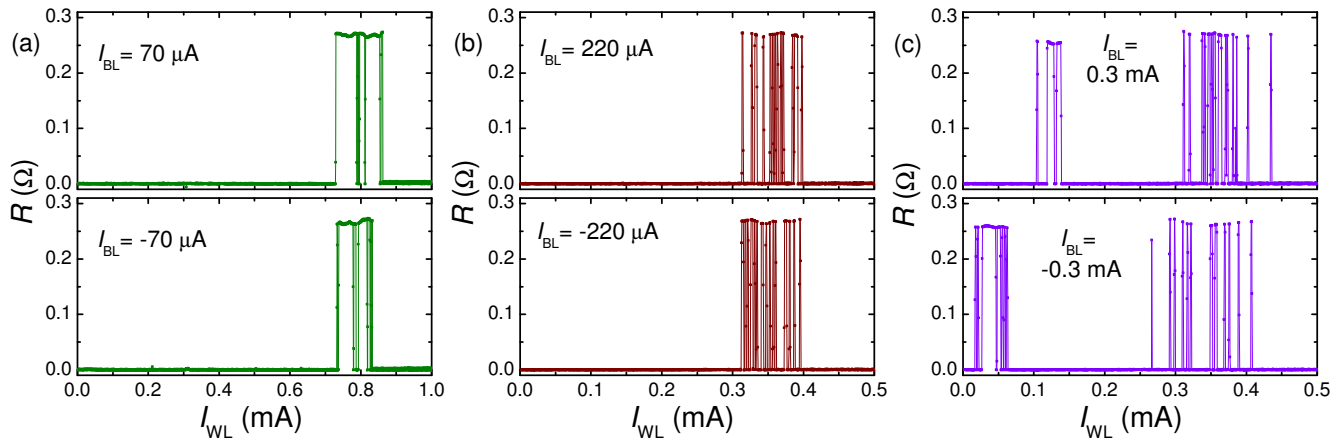


FIG. 5. **Word and bit-line operation of the $1 \times 1 \mu\text{m}^2$ cell.** The readout junction resistance is shown as a function of the positive WL pulse amplitude, I_{WL} , for fixed amplitudes of the BL current. (a) $I_{\text{BL}} = \pm 70 \mu\text{A}$; (b) $I_{\text{BL}} = \pm 220 \mu\text{A}$; and (c) $I_{\text{BL}} = \pm 300 \mu\text{A}$. A significant reduction of the threshold WL current is observed upon simultaneous application of the BL current. Measurements were performed at $T = 5.85 \text{ K}$ and $H = 0$.

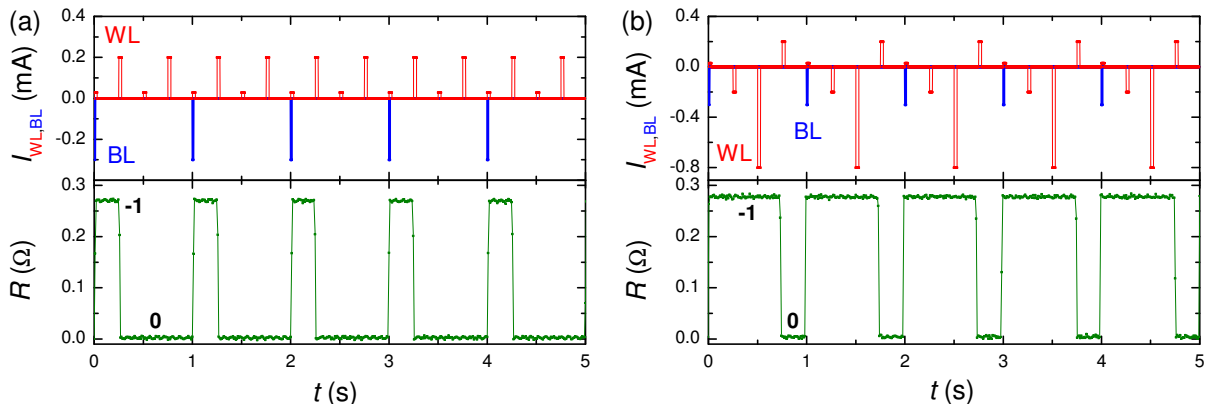


FIG. 6. **Demonstration of a simultaneous word and bit-line operation of the $1 \times 1 \mu\text{m}^2$ cell.** (a) Writing an antivortex by combined pulses $I_{\text{BL}} = -300 \mu\text{A}$ and $I_{\text{WL}} = 29 \mu\text{A}$; and erasing by a WL pulse $200 \mu\text{A}$. (b) Similar write and erase pulses as in (a) with additional intermediate WL pulses. It is seen that the negative WL pulses do not change the -1 state because they tend to write an antivortex and the trap is already occupied. In all figures, top panels show time sequences of WL (red) and BL (blue) pulses. Bottom panels show a simultaneously measured ac-resistance of the readout junction. Measurements were performed at $T = 5.85 \text{ K}$ and $H = 0$.

III. DISCUSSION

We demonstrated that the planar AVRAM cell can be straightforwardly scaled down to $\sim 1 \times 1 \mu\text{m}^2$. Furthermore, threshold currents for miniaturized cells are significantly reduced, compared to larger cells, studied in Ref. [7]. We observe that the threshold WL current is approximately proportional to the width of the WL electrode. This is expected because vortex motion occurs when the transport current density exceeds the depinning current density. Consequently, upon miniaturization, the threshold current scales down proportional to the size. Therefore, AVRAM cells do not suffer from the problem of threshold current enhancement upon miniaturization, as SQUIDS in RSFQ. This proves that AVRAM cells are

indeed scalable.

The area of the presented $\sim 1 \times 1 \mu\text{m}^2$ cell is already ~ 100 times smaller than for the state of the art RSFQ cells [11, 12]. But this is not the ultimate limit. Miniaturization of the AVRAM cell is limited by the stability of AV in a mesoscopic superconducting electrode. In order to work as a memory bit, the vortex should be persistent in the trap at zero magnetic field. Metastable vortex configurations in mesoscopic superconductors have been intensively studied and are well understood [38–44]. The trap plays an important role in stabilizing the vortex. It changes the electrode topology and creates a sharp pinning potential, which stabilizes otherwise energetically unfavorable ± 1 vortex states at zero field. The tendency of the vortex to spontaneously jump out of the electrode

can be viewed as the consequence of an attractive interaction with an image antivortex outside the electrode [35]. From Fig. 2 (a) it can be seen that for the studied $1 \times 1 \mu\text{m}^2$ device the nearest to the trap edge corresponds to the readout JJ, 240 nm away. Apparently, this distance is sufficient for preventing a spontaneous vortex exit. Consequently, the cell can be straightforwardly miniaturized to twice this size, i.e., to $\sim 500 \times 500 \text{ nm}^2$.

Generally, vortices can exist in superconductors with sizes down to the coherence length, ξ . However, the smaller is the size, the larger is the relative energy cost of a vortex at zero field. Our sputtered Nb films have a short coherence length of $\xi(0) = 14 \text{ nm}$ and a London penetration depth, $\lambda_L(0) \simeq 100 \text{ nm}$ [45]. Therefore, we anticipate that further miniaturization down to $\sim 100 \text{ nm}$ should be feasible.

We have emphasized that a specific geometrical asymmetry is needed for controllable vortex manipulation. This is particularly important for submicron AVRAM cells, which are in the mesoscopic limit. Geometry (sizes and shapes) is playing a crucial role for vortex states in mesoscopic superconductors [38–44]. Proper design of the cell geometry (the trap and the electrode) would be needed for optimization of AVRAM.

In this work we introduced several small but important improvements in the cell design, compared to the initial prototype [7]. First, the film structure was reduced to a single Nb film (compared to a bilayer superconductor/normal metal or superconductor/ferromagnet) and the readout junction structure became of a variable-thickness-bridge type (compared to proximity-coupled SNS or SFS JJs). Apart from a bare simplification, this leads to a major enhancement of the $I_c R_n$ product, reaching almost 1 mV at low T [33]. This results in a proportional enhancement of the readout voltage [32], which is very important for device applications.

Most importantly, we have consciously engineered geometrical asymmetry. An easy track for vortex manipulation was made at one side of the trap. This led to

improved controllability and reduced threshold currents. The analysis in Table I confirms that the track works and vortices indeed follow this route. The achieved threshold currents, as low as $150 \mu\text{A}$, are optimal for practical AVRAM. Further reduction would jeopardize the non-destructive readout and lead to smaller readout signals. Other geometrical features that help to guide vortex motion were also suggested in the literature [43, 44] and could be implemented, if necessary.

IV. CONCLUSIONS

We have studied single-bit AVRAM cells and arrived to three main conclusions.

(i) The planar AVRAM cell design is straightforwardly scalable to submicron sizes. The threshold current is reducing upon miniaturization, approximately proportionally to the size, thus obviating the problem of SQUID-based RSFQ cells. Robust, non-volatile operation at zero magnetic field was demonstrated for a $\sim 1 \times 1 \mu\text{m}^2$ cell. Its area is approximately 100 times smaller than for the state of the art RSFQ cells.

(ii) We emphasized the importance of a conscious geometrical design of the cell geometry. A specific geometrical asymmetry (an easy track) was introduced in our cells. It enabled controllable and comprehensible operation of the cell.

(iii) Word and bit line operation exhibits a profound cooperative effect, reducing the total threshold current. The smaller combined WL+BL currents reduce chances of affecting other cells at the same WL. This can improve the selectivity of cell addressing in a multibit RAM.

We conclude that planar AVRAM cells are promising candidates for the creation of VLSI-compatible superconducting memory. The achieved one square micron area is an important milestone and a significant step forward in this direction.

-
- [1] F. Arute, K. Arya, R. Babbush, D. Bacon, J. C. Bardin, R. Barends, R. Biswas, S. Boixo, F. G. Brandao, D. A. Buell, et al., Quantum supremacy using a programmable superconducting processor, *Nature* **574**, 505 (2019).
 - [2] A. Kandala, K. Temme, A. D. Corcoles, A. Mezzacapo, J. M. Chow, and J. M. Gambetta, Error mitigation extends the computational reach of a noisy quantum processor, *Nature* **567**, 491 (2019).
 - [3] E. A. Borodiansky and V. M. Krasnov, Josephson emission with frequency span 1-11 THz from small $\text{Bi}_2\text{Sr}_2\text{CaCu}_2\text{O}_{8+\delta}$ mesa structures. *Nat. Commun.* **8**, 1742 (2017).
 - [4] D. S. Holmes, A.L. Ripple, and M.A. Manheimer, Energy-efficient superconducting computing—power budgets and requirements. *IEEE Trans. Appl. Supercond.* **23**, 1701610 (2013).
 - [5] T. Ortlepp, and T. Van Duzer, Access time and power dissipation of a model 256-bit single flux quantum RAM. *IEEE Trans. Appl. Supercond.* **24**, 1300307 (2014).
 - [6] M. A. Manheimer, Cryogenic computing complexity program: Phase I introduction. *IEEE Trans. Appl. Supercond.*, **25**, 1301704 (2015).
 - [7] T. Golod, A. Iovan, and V. M. Krasnov, Single Abrikosov vortices as quantized information bits. *Nature Commun.* **6**, 8628 (2015).
 - [8] I. I. Soloviev, N. V. Klenov, S. V. Bakurskiy, M. Y. Kupriyanov, A. L. Gudkov and A. S. Sidorenko, Beyond Moore’s technologies: operation principles of a superconductor alternative. *Beilstein J Nanotechnol.* **8**, 2689 (2017).
 - [9] I. M. Dayton, T. Sage, E. C. Gingrich, M. G. Loving, T. F. Ambrose, N. P. Siwak, S. Keebaugh, C. Kirby, D. L. Miller, A. Y. Herr, Q. P. Herr, O. Naaman, Experimental demonstration of a Josephson magnetic memory cell

- with a programmable π -junction. *IEEE Magn. Lett.* **9**, 3301905 (2018).
- [10] S. K. Tolpygo, V. Bolkhovskiy, R. Rastogi, S. Zarr, A. L. Day, E. Golden, T. J. Weir, A. Wynn, and L. M. Johnson, Advanced Fabrication Processes for Superconductor Electronics: Current Status and New Developments. *IEEE Trans. Appl. Supercond.* **29**, 1102513 (2019).
- [11] V. K. Semenov, Y. A. Polyakov, and S. K. Tolpygo, Very Large Scale Integration of Josephson-Junction-Based Superconductor Random Access Memories. *IEEE Trans. Appl. Supercond.* **29**, 1302809 (2019).
- [12] L. Chen, L. Wu, Y. Wang, Y. Pan, D. Zhang, J. Zeng, X. Liu, L. Ma, W. Peng, Y. Wang, J. Ren, and Z. Wang, Miniaturization of the Superconducting Memory Cell via a Three-Dimensional Nb Nanosuperconducting Quantum Interference Device. *ASC Nano* **14**, 11002-11008 (2020).
- [13] K.K. Likharev, Dynamics of Josephson junctions and circuits. (Gordon and Breach Sci. Publ., 1986).
- [14] S. Nagasawa, K. Hinode, T. Satoh, Y. Kitagawa and M. Hidaka, Design of all-dc-powered high-speed single flux quantum random access memory based on a pipeline structure for memory cell arrays. *Supercond. Sci. Technol.* **19**, S325–S330 (2006).
- [15] T. Ortlepp, Ariando, O. Mielke, C. J. M. Verwijs, K. F. K. Foo, H. Rogalla, F. H. Uhlmann, and H. Hilgenkamp, Flip-flopping fractional flux quanta. *Science* **312**, 1495 (2006).
- [16] V. I. Zdravkov, D. Lenk, R. Morari, A. Ullrich, G. Obermeier, C. Müller, H.-A. Krug von Nidda, A. S. Sidorenko, S. Horn, R. Tidecks, and L. R. Tagirov. Memory effect and triplet pairing generation in the superconducting exchange biased $\text{Co}/\text{CoO}_x/\text{Cu}_{41}\text{Ni}_{59}/\text{Nb}/\text{Cu}_{41}\text{Ni}_{59}$ layered heterostructure. *Appl. Phys. Lett.* **103**, 062604 (2013).
- [17] I. V. Vernik, V. V. Bol'ginov, S. V. Bakurskiy, A. A. Golubov, M. Y. Kupriyanov, V. V. Ryazanov and O. A. Mukhanov, Magnetic Josephson junctions with superconducting interlayer for cryogenic memory. *IEEE Trans. Appl. Supercond.* **23**, 1701208 (2013).
- [18] E. Goldobin, H. Sickinger, M. Weides, N. Ruppelt, H. Kohlstedt, R. Kleiner and D. Koelle, Memory cell based on a φ -Josephson junction. *Appl. Phys. Lett.* **102**, 242602 (2013).
- [19] B. Baek, W.H. Rippard, S. P. Benz, S. E. Russek, P. D. Dresselhaus, Hybrid superconducting-magnetic memory device using competing order parameters. *Nat. Commun.* **5**, 3888 (2014).
- [20] A. Murphy, D. Averin and A. Bezryadin, Nanoscale superconducting memory based on the kinetic inductance of asymmetric nanowire loops. *New J. Phys.* **19**, 063015 (2017).
- [21] B. M. Niedzielski, T. J. Bertus, J. A. Glick, R. Loloee, W. P. Pratt, and N. O. Birge, Spin-valve Josephson junctions for cryogenic memory. *Phys. Rev. B* **97**, 024517 (2018).
- [22] I. P. Nevirkovets, and O. A. Mukhanov, Memory Cell for High-Density Arrays Based on a Multiterminal Superconducting-Ferromagnetic Device. *Phys. Rev. Appl.* **10**, 034013 (2018).
- [23] A. E. Madden, J. C. Willard, R. Loloee and N. O. Birge, Phase controllable Josephson junctions for cryogenic memory. *Supercond. Sc. Technol.* **32**, 015001 (2019).
- [24] R. de Andrés Prada, T. Golod, O. M. Kapran, E. A. Borodianskyi, Ch. Bernhard, and V. M. Krasnov, Memory-functionality superconductor/ferromagnet/superconductor junctions based on the high- T_c cuprate superconductors $\text{YBa}_2\text{Cu}_3\text{O}_{7-x}$ and the colossal magnetoresistive manganite ferromagnets $\text{La}_{2/3}\text{X}_{1/3}\text{MnO}_{3+\delta}$ ($X = \text{Ca}, \text{Sr}$). *Phys. Rev. B* **99**, 214510 (2019).
- [25] N. Ligato E. Strambini, F. Paolucci, and F. Giazotto, Preliminary demonstration of a persistent Josephson phase-slip memory cell with topological protection. *Nat. Commun.* **12**, 5200 (2021).
- [26] L. N. Karelina, R. A. Hovhannisyan, I. A. Golovchanskiy, V. I. Chichkov, A. Ben Hamida, V. S. Stolyarov, L. S. Uspenskaya, Sh. A. Erkenov, V. V. Bolginov, and V. V. Ryazanov, Scalable memory elements based on rectangular SISFS junctions. *J. Appl. Phys.* **130**, 173901 (2021).
- [27] B. A. Butters, R. Baghdadi, M. Onen, E. A. Toomey, O. Medeiros, and K. K. Berggren, A scalable superconducting nanowire memory cell and preliminary array test. *Supercond. Sci. Technol.* **34**, 035003 (2021).
- [28] S. Alam, Md S. Hossain, S. R. Srinivasa, and A. Aziz, Cryogenic Memory Technologies. *ArXiv:2111.09436*.
- [29] R. Fermin, N. M. A. Scheinowitz, J. Aarts, and K. Lahabi, Mesoscopic superconducting memory based on bistable magnetic textures. *Phys. Rev. Research* **4**, 033136 (2022).
- [30] W. J. Gallagher, and S. S. P. Parkin, Development of the magnetic tunnel junction MRAM at IBM: from first junctions to a 16-Mb MRAM demonstrator chip. *IBM J. Res. Dev.* **50**, 5–23 (2006).
- [31] T. Golod, R. A. Hovhannisyan, O. M. Kapran, V. V. Dremov, V. S. Stolyarov, and V. M. Krasnov, Reconfigurable Josephson Phase Shifter. *Nano Lett.* **21**, 5240-5246 (2021).
- [32] T. Golod, and V. M. Krasnov, Demonstration of a superconducting diode-with-memory, operational at zero magnetic field with switchable nonreciprocity. *Nat. Commun.* **13**, 3658 (2022).
- [33] S. Yu. Grebenchuk, R. Cattaneo, and V. M. Krasnov, Nonlocal Long-Range Synchronization of Planar Josephson-Junction Arrays. *Phys. Rev. Appl.* **17**, 064032 (2022).
- [34] Supplementary material...
- [35] T. Golod, A. Pagliero, and V. M. Krasnov, Two mechanisms of Josephson phase shift generation by an Abrikosov vortex. *Phys. Rev. B* **100**, 174511 (2019).
- [36] T. Golod, A. Rydh, and V. M. Krasnov, Detection of the Phase Shift from a Single Abrikosov Vortex. *Phys. Rev. Lett.* **104**, 227003 (2010).
- [37] V. M. Krasnov, Josephson junctions in a local inhomogeneous magnetic field. *Phys. Rev. B* **101**, 144507 (2020).
- [38] A. Bezryadin, A. Buzdin, and B. Pannetier, Phase diagram of multiply connected superconductors: A thin-wire loop and a thin film with a circular hole. *Phys. Rev. B* **51**, 3718 (1995).
- [39] A. K. Geim, I. V. Grigorieva, S. V. Dubonos, J. G. S. Lok, J. C. Maan, A. E. Filippov, and F. M. Peeters, Phase transitions in individual sub-micrometre superconductors. *Nature* **390**, 259 (1997).
- [40] G. R. Berdiyev, B. J. Baelus, M. V. Milosevic, and F. M. Peeters, Stability and transition between vortex configurations in square mesoscopic samples with antidots. *Phys. Rev. B* **68**, 174521 (2003).
- [41] L. F. Chibotaru, A. Ceulemans, M. Morelle, G. Teniers, C. Carballeira, and V. V. Moshchalkov, Ginzburg–Landau description of confinement and quantization effects in mesoscopic superconductors. *J. Math.*

- Phys.* **46**, 095108 (2005).
- [42] M.V. Milosevic, A. Kanda, S. Hatsumi, F.M. Peeters, and Y. Ootuka, Local current injection into mesoscopic superconductors for the manipulation of quantum states. *Phys. Rev. Lett.* **103**, 217003 (2009).
- [43] A. V. Kapra, V. R. Misko, D. Y. Vodolazov and F. M. Peeters, The guidance of vortex–antivortex pairs by in-plane magnetic dipoles in a superconducting finite-size film. *Supercond. Sci. Technol.* **24**, 024014 (2011).
- [44] I. G. de Oliveira, Magnetic Flux Penetration in a Mesoscopic Superconductor with a Slit. *J. Supercond. Nov. Magn.* **27**, 1143–1152 (2014).
- [45] A. Zeinali, T. Golod, and V. M. Krasnov, Surface superconductivity as the primary cause of broadening of superconducting transition in Nb films at high magnetic fields. *Phys. Rev. B* **94**, 214506 (2016).